ASME Letters in Dynamic Systems and Control
Online journal at:
https://asmedigitalcollection.asme.org/lettersdynsys

# Multi-Track Melt Pool Width Modeling in Powder Bed Fusion Additive Manufacturing

**Dan Wang**[1]
Western Digital Corp,
San Jose, CA 95119
e-mail: daw1230@uw.edu

**Xu Chen**
Department of Mechanical Engineering,
University of Washington,
Seattle, WA 98195
e-mail: chx@uw.edu

*While powder bed fusion (PBF) additive manufacturing offers many advantages and exciting applications, its broader adoption is hindered by issues with reliability and variations during the manufacturing process. To address this, researchers have identified the importance of using both finite element modeling and control-oriented modeling to predict and improve the quality of printed parts. In this paper, we propose a novel control-oriented multi-track melt pool width model that utilizes the superposition principle to account for the complex thermal interactions that occur during PBF. We validate the effectiveness of the model by applying a finite element model of the thermal fields in PBF.*
[DOI: 10.1115/1.4063475]

*Keywords: modeling, control implementation, powder bed fusion, additive manufacturing, control applications, dynamics and control, mechatronics*

## 1 Introduction

Additive manufacturing (AM) differs from conventional subtractive machining as it creates a part by adding material layer by layer, directly from a digital model. Powder bed fusion (PBF) is a specific AM technique that uses high-precision lasers or electron beams as the energy source to fuse polymeric or metallic powder materials together. While PBF has revolutionized the fabrication of complex parts, there are still challenges to its wider adoption. These challenges include issues with reliability and in-process variations caused by uncertain laser-material interactions, environmental vibrations, powder recycling, imperfect interactions of mechanical components, and the recursive thermal histories of materials [1–5].

In PBF, a typical part is built from thousands of thin layers, as shown in Fig. 1. Each layer is created by regulating the energy beam to follow trajectories predetermined in a slicing process based on the part geometry. Once a layer is finished printing, a new thin layer of powder is spread on top, and the process repeats. Modeling this complex dynamic system (Fig. 1) is crucial for understanding and controlling PBF and related techniques. Researchers use finite element modeling to explore energy deposition mechanisms, and control-oriented modeling to build mathematical models that can regulate in-process variations. For instance, Refs. [1,6–8] adopt finite element modeling to investigate the effects of various scan configurations on the thermal fields of powder bed, the geometries of melt pool, and the mechanical properties of printed parts. In control-oriented modeling, Refs. [9–12] employ the low-order system models and further build the nonlinear submodels to cover more process dynamics. Based on these models, subsequent control algorithms such as PID control [13], sliding mode control [11], predictive control [9], repetitive control [2,14], iterative learning-based control [15], and iterative simulation-based control [4,16] have proven effective in improving the dimensional accuracy of printed parts.

This paper presents a novel approach to modeling and examining PBF by combining finite element modeling and control-oriented modeling. First, we develop a finite element model (FEM) to look into the intricate thermal interactions that occur during the PBF process. The FEM then serves as a simulation platform for gathering data and identifying parameters for the proposed modeling schemes. In contrast to the typically used low-order system models, we develop a physics-based analytical model for control-oriented modeling that accounts for the complex dynamic behavior of melt pool width during multi-track PBF process. The proposed control-oriented multi-track model is formulated by applying superposition to a single-track model derived from the Rosenthal equation, with melt pool width as the output. We validate the accuracy of the multi-track melt pool width model using FEM and demonstrate that the developed model can effectively represent the key characteristics of the convoluted multi-track PBF process.

The remainder of this paper is structured as follows. In Sec. 2, we build the FEM of the thermal fields in PBF. Section 3 explores the preliminary physics related to melt pool width. Section 4 develops and analyzes the primary multi-track melt pool width model. Finally, Sec. 5 concludes the paper.

## 2 Finite Element Model of Thermal Fields in Powder Bed Fusion

In this section, we develop and refine an FEM to simulate the thermal fields in PBF. The FEM accounts for surface convection, surface radiation, conduction, and latent heat of fusion. To maintain computational efficiency and without compromising generality, we exclude the effects of evaporation, fluid flow, and Marangoni force

[1]Corresponding author.
Paper Presented at the 2023 Modeling, Estimation, and Control Conference (MECC 2023), Lake Tahoe, NV, Oct. 2–5. Paper No. MECC2023-18.
Manuscript received July 8, 2023; final manuscript received August 30, 2023; published online October 5, 2023. Assoc. Editor: Loucas Louca.

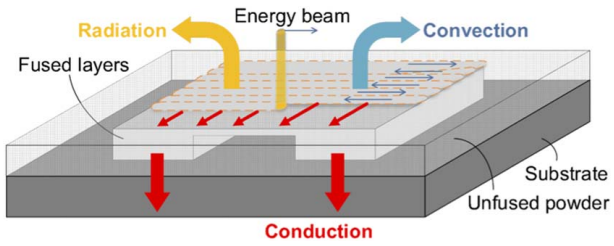


**Fig. 1 Schematic of heat transfer in PBF**

when constructing the FEM using COMSOL MULTIPHYSICS 5.3A software. The governing equation for the conduction heat flow is

$$\rho c_p \frac{\mathrm{d}T(x,\ y,\ z,\ t)}{\mathrm{d}t} = \nabla \cdot (k \nabla T(x,\ y,\ z,\ t)) + q_s \tag{1}$$

where $T$ is the temperature distribution, $k$ the thermal conductivity, $c_p$ the specific heat capacity, $\rho$ the effective density, and $q_s$ the rate of local internal energy generated per unit volume [17].

In this study, we assume a uniform distribution of the initial temperature $T(x,\ y,\ z,\ 0) = T_0$. When the substrate (left plot of Fig. 2) is designed to be large enough compared to the heat affected zone, one boundary condition is established by assuming the bottom of the substrate ($z = h_b$) has no heat loss: $-k \left.\dfrac{\partial T}{\partial z}\right|_{z=h_b} = 0$. The other boundary condition considers surface conduction, convection, and radiation:

$$-k \left.\frac{\partial T}{\partial z}\right|_{z=0} = -Q + h_c(T - T_0) + \varepsilon \sigma_B (T^4 - T_0^4), \tag{2}$$

where $Q$ is the input heat flux, $h_c$ the convection heat transfer coefficient, $\varepsilon$ the emissivity, and $\sigma_B$ the Stefan–Boltzmann constant. Here, we assume $Q$ has a Gaussian laser beam profile: $Q \approx \dfrac{2q}{\pi R^2} \mathrm{e}^{-\frac{2r^2}{R^2}}$, where $q$ is the laser power, $R$ the effective laser beam radius, and $r$ the radial distance from a certain point to the center of the laser spot.

We employ temperature-dependent thermal properties $k$, $c_p$, and $\rho$ for both solid and liquid materials. Then, we calculate the thermal properties of the powder material based on the porosity of the solid material. To account for the latent heat of fusion, we introduce the effective heat capacity. The left plot of Fig. 2 displays the bidirectional scan strategy and the built geometry blocks that consist of a substrate and a thin layer of powder bed. The right plot of Fig. 2 illustrates the simulated surface temperature profile at 0.14 s, where the isotherm of $T = T_m$ depicts the melt pool geometry and $T_m$ is the melting point. For more information regarding the thermal properties, process parameters, and meshing scheme utilized in this FEM, please refer to Ref. [4], where it has been experimentally validated.

The developed FEM functions as a simulation platform for predicting the thermal fields of the powder bed throughout the multitrack PBF process. The finite element results are shown in Fig. 3, as well as in the top plots of Figs. 6 and 8. We observe that the start of each track has larger melt pool widths than the rest of the track. This is because in bidirectional scanning, when the energy beam approaches the end of one track, the large latent heat does not have enough time to dissipate out before the next track starts. Later on we will use the data (e.g., melt pool width) generated from the FEM to identify and verify the proposed analytical model. Specifically, we obtain the melt pool width from the FEM-predicted temperature distribution by searching the isotherm of $T = T_m$ for the maximum width.

## 3 Preliminaries

The Rosenthal equation is commonly used in the context of additive manufacturing to estimate the temperature distribution during the manufacturing process. This equation relates the temperature at a specific point in a material to the process parameters such as laser power, scan speed, and material properties.

When a moving point laser source is acting on a large thick plate, the analytical solution of Eq. (1) in the steady-state is the Rosenthal equation [17]

$$T(\xi,\ y,\ z) = T_0 + T_r \tag{3}$$

$$T_r = \frac{q}{2\pi k r} \mathrm{e}^{-\frac{u_x(r+\xi)}{2\kappa}} \tag{4}$$

where $(\xi,\ y,\ z)$ is a coordinate system attached to the moving source, $u_x$ the scan speed, $r = \sqrt{\xi^2 + y^2 + z^2}$, and $\kappa = k/(\rho c_p)$.

The derivation of the Rosenthal equation involves making certain assumptions and simplifications. First, the material's physical coefficients such as $k$, $\rho$, and $c_p$ are assumed to be independent of temperature. The use of average values of these coefficients provides a reasonable approximation and enables a closed-form solution to be obtained. Second, the internal heat generation is neglected, i.e., $q_s = 0$. Third, the workpiece material is assumed to be homogeneous and isotropic. Additionally, when the powder bed is processed long enough, a quasi-stationary state is presumed to be reached, i.e., the temperature undergoes no change with time in the moving coordinate system $(\xi,\ y,\ z)$. Moreover, a point heat source is used instead of a Gaussian distribution. Finally, the effect of latent heat of fusion is considered negligible since the absorbed latent heat evolves later on.

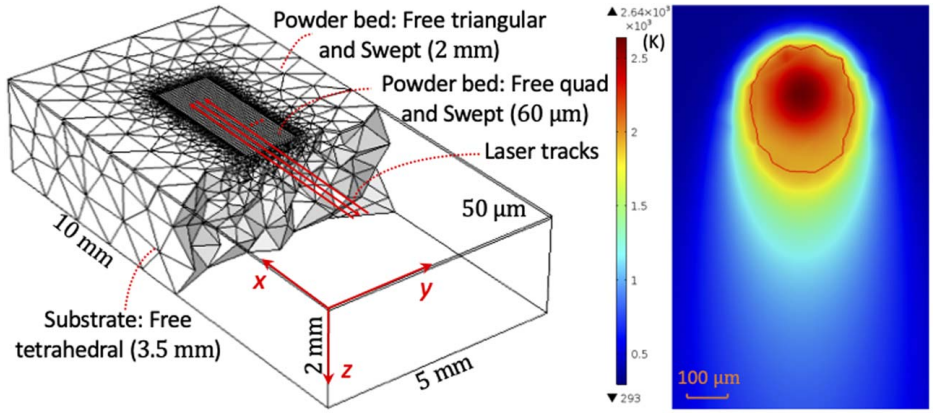


**Fig. 2 Left: powder bed and substrate with selective meshing scheme. Right: surface temperature distribution at $t = 0.14$ s. The lined isotherm indicates $T = T_m$.**

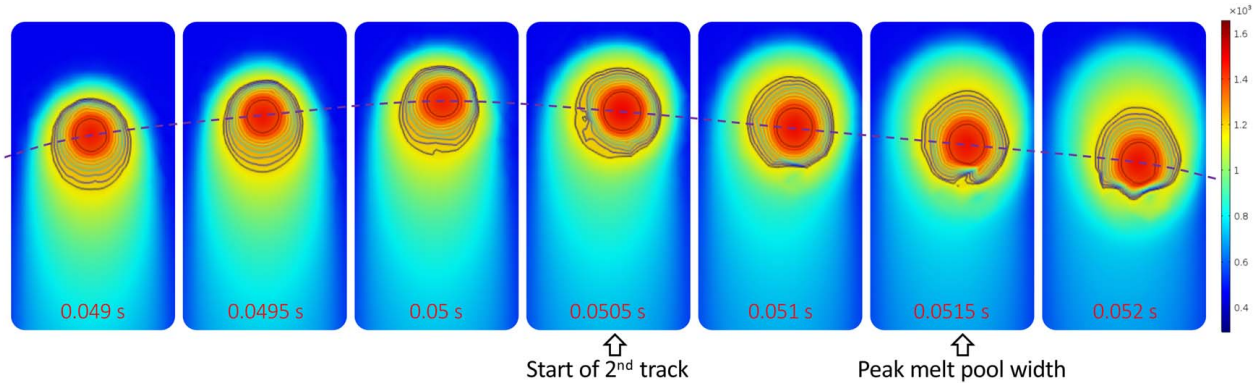


**Fig. 3 FEM result: surface temperature distributions showing melt pool width evolution**

It's worth pointing out that the Rosenthal equation is not directly derived from Green's functions or probability density function (PDF) kernels. The Rosenthal equation is a simplified heat conduction equation that takes into account factors like heat generation, heat conduction, and convective cooling, but it's derived through simplifications and assumptions specific to the additive manufacturing process. Green's functions or PDF kernels are used in more general mathematical and physical contexts to solve differential equations, including heat conduction equations, but their direct connection to the Rosenthal equation in additive manufacturing is not common.

From the Rosenthal equation in Eq. (3), the analytical expression of the steady-state melt pool width $w$ for a single track is derived in Ref. [18] and further in Ref. [4]:

$$q = \pi k(T_m - T_0)w + e\pi\rho c_p(T_m - T_0)u_x w^2/8 \tag{5}$$

Assumptions in deriving Eq. (5) include

- $-\dfrac{\ln(r^*V)}{r^*M} \approx 0$, where $M = \dfrac{u_x}{2\kappa}$, $V = \dfrac{2\pi k(T_m - T_0)}{q}$, and $r^*$ represents the value of $r$ at the melt pool width.
- $r^*M \gg 1$.
- The approximation of $q$ is improved by including the zero-speed power, i.e., the first term on the right-hand side of Eq. (5).

The assumptions hold reasonably well for all alloys except AlSi10Mg under typical PBF configurations [18].

## 4 Multi-Track Melt Pool Width Model

Melt pool width is a crucial parameter for monitoring part properties during PBF manufacturing. Maintaining a user-defined reference value for melt pool width is essential to achieving uniform part quality [19]. To fulfill this requirement, we present a novel analytical model that emulates the dynamic behavior of melt pool width during the multi-track PBF process. The application of this multi-track melt pool width model can aid in developing control algorithms that mitigate process variations and ensure consistent part quality. In this section, we implement the superposition principle to model the evolution of the multi-track melt pool width, based on the single track expression in Eq. (5). The key idea is that the cumulative thermal effect of previous tracks on the current track is reflected on the increasing initial temperature $T_0$.

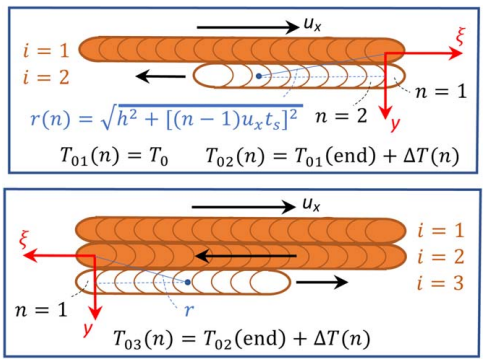


**Fig. 4 Illustration of initial temperature computation**

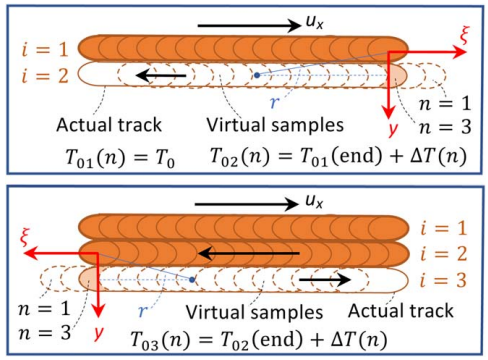


**Fig. 5 After shift: illustration of initial temperature computation**

**Table 1 Parameter values**

| Name | Symbol | Value |
|---|---|---|
| Laser power | $q$ | 60 W |
| Scan speed | $u_x$ | 100 mm/s |
| Melting point | $T_m$ | 1923.15 K |
| Sampling time | $t_s$ | 0.5 ms |
| Ambient Temperature | $T_{amb}$ | 293.15 K |
| No. of samples per track | $N$ | 100 |
| Hatch spacing | $h$ | 60 $\mu$m |
| Thermal properties | $k$, $\rho$, $c_p$ | [12] |

To explain the proposed analytical model in detail, we provide a step-by-step procedure below. The melt pool width of the first track $w_1$ can be directly calculated by Eq. (5) with $T_0 = T_{01} = T_{amb}$, where $T_{01}$ indicates the initial temperature of every sample on the first track and equals the ambient temperature $T_{amb}$. Parameters $q$, $u_x$, $k$, $\rho$, and $c_p$ are set to be constant. When the laser point reaches the end of the first track, for every sample on the second track as shown in Fig. 4, $\xi = (n-1)u_x t_s$, $y = h$, and $z = 0$, where $n$ is the sample number, $t_s$ the sampling time, and $h$ the hatch spacing. Furthermore, we have $T_1(\xi, h, 0) = T_{01}(N) + T_r(n)$ from Eq. (3), where $T_1$ is the temperature distribution of the laser point at the track end

and $N$ is the total number of samples per track. Here, $T_{01}(N)$ indicates the initial temperature of the last sample at the first track. The residual thermal effect of the first track on the second track are reflected on the initial temperature of every sample on the second track: $T_{02}(n) = T_1(\xi, h, 0) = T_{01}(N) + T_r(n)$. Then with $T_0 = T_{02}$, we can calculate the melt pool width of the second track $w_2(n)$ from Eq. (5). Similarly, for the $i$ th track, we have $T_{0i}(n) = T_{0(i-1)}(N) + T_r(n)$, and the melt pool width $w_i(n)$ is the solution of Eq. (5) with $T_0 = T_{0i}$.

**Algorithm 1** Multi-track melt pool width modeling

**Require:** number of tracks $M$, number of samples per track $N$, laser power $q$, scan speed $u_x$, melting point $T_m$, ambient temperature $T_{amb}$, sampling time $t_s$, hatch spacing $h$, thermal properties $k$, $\rho$, $c_p$, sample shift $n_p$, and tuning parameters $\alpha$, $\beta$

$i \leftarrow 1$
$T_{01} \leftarrow T_{amb}$
**while** $i <= M$ **do**
  $n \leftarrow 1$
  **while** $n <= N$ **do**
    **if** $n < n_p$ **then**
      $\xi = \beta\,(n - n_p)u_x t_s$
    **else**
      $\xi = (n - n_p)u_x t_s$
    **end if**
    $r = \sqrt{h^2 + \xi^2}$
    Calculate $T_r(n)$ from Eq. (4)
    $T_{0i}(n) = T_{0(i-1)}(N) + T_r(n)/\alpha$
    Calculate $w_i(n)$ by (5) with $T_0 = T_{0i}$
    $n \leftarrow n + 1$
  **end while**
  $i \leftarrow i + 1$
**end while**

For an individual track, we notice that the melt pool width reaches its peak value a few samples after the track start, specifically at $n = n_p$. For example, $n_p = 3$ in Fig. 3. On the other hand, from the analytical multi-track model, the melt pool width reaches its peak value at the track start since $n = 1$, $\xi = (n-1)u_x t_s = 0$, $T_r$ in Eq. (4) peaks, and then $T_{0i}$ peaks. To address the mismatch, we make an adaptation to the proposed model by shifting the virtual laser spots out by $n_p - 1$ samples (see Fig. 5) and introducing a tuning parameter $\beta$ for the first $n_p - 1$ samples (as in Algorithm 1). Furthermore, to add more design flexibility, we reformulate $T_{0i}$ as $T_{0i}(n) = T_{0(i-1)}(N) + T_r(n)/\alpha$ by introducing another tuning parameter $\alpha$. Algorithm 1 outlines the fundamental steps of the proposed analytical model for predicting the melt pool width during the multi-track PBF process.

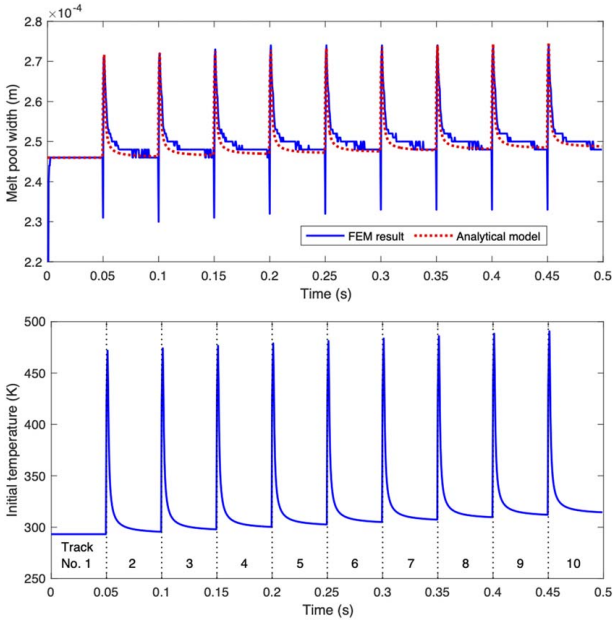


**Fig. 6 Ten tracks: top: melt pool width from analytical model and FEM, bottom: analytical $T_{0i}$**

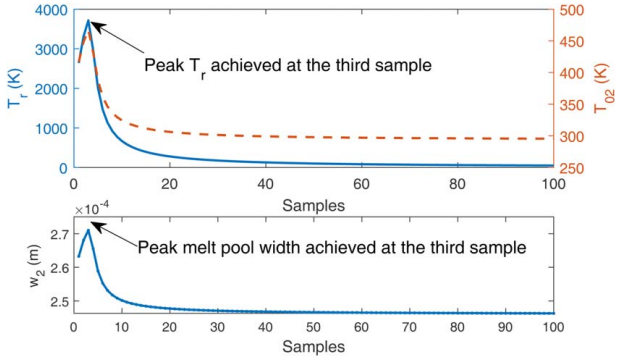


**Fig. 7 Identified $T_r$, $T_{02}$, and $w_2$ after shift**

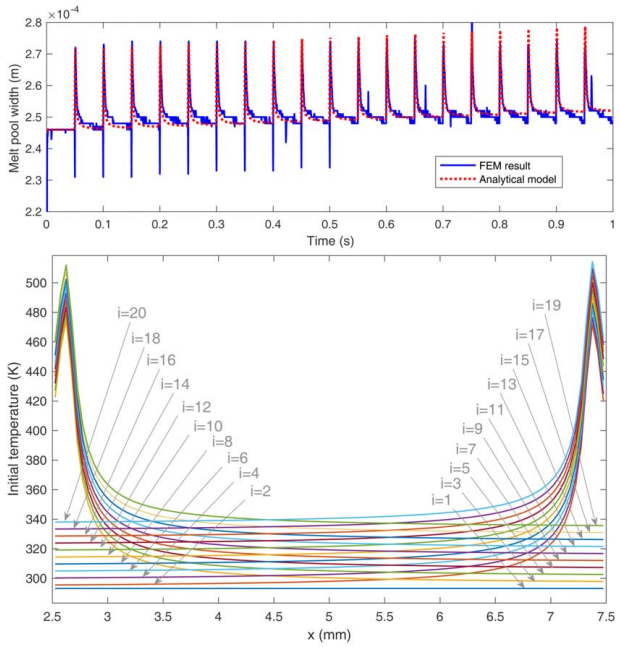


**Fig. 8 Twenty tracks: top: melt pool width from analytical model and FEM, bottom: analytical $T_{0i}$**

We employ the FEM built in Sec. 2 to simulate the evolution of the melt pool width among multiple tracks. Using the ten-track FEM data in Fig. 6, we identify the parameters in the proposed multi-rack melt pool width model as $n_p = 3$, $\alpha = 20.8$, and $\beta = 0.5$. The other parameter values can be found in Table 1. Figure 7 shows the resulted $T_r$, $T_{02}$, and $w_2$, where the analytical melt pool width peaks at the third sample after the shift. Furthermore, we compare in Fig. 8 the twenty-track melt pool results from the identified analytical model and the FEM. From the top plots of Figs. 6 and 8, we can tell that the proposed multi-track model can effectively capture the spikes at the start of each track. Moreover, the model can catch the increasing trend of the melt pool width as the track number increases. This is due to the fact that the initial temperature profile $T_{0i}$ increases with the track number, as shown in the bottom plots of Figs. 6 and 8. Overall, the proposed model's melt pool width results closely match those of the FEM, with a difference of 5 $\mu$m. In addition, compared to FEM, the proposed model

reduces the computational burden to a bare minimum. When modeling the ten-track PBF process as in Fig. 6, it takes 4.5 h using FEM [4] and only seconds using the proposed multi-track melt pool width model. Although the FEM has been experimentally validated in Ref. [4], our future endeavors will involve further verification of the proposed model through the PBF experiments directly.

## 5 Conclusion

In this paper, we present a comprehensive approach to analyze the melt pool width during the multi-track PBF process. First, we construct a FEM to simulate the thermal fields of PBF. Next, we develop a multi-track analytical model by applying the superposition principle to a single-track melt pool width model derived from the Rosenthal equation. Based on the FEM data, we identify the parameters and validate the effectiveness of the proposed model. The results demonstrate that the proposed analytical model can effectively be catching the complex dynamics of melt pool width that occur during the multi-track PBF process.


## Acknowledgment

This work is supported by the National Science Foundation under Award No. 1953155.


## Conflict of Interest

There are no conflicts of interest.

## Data Availability Statement

The datasets generated and supporting the findings of this article are obtainable from the corresponding author upon reasonable request.

## References


[1] Liao, S., Golgoon, A., Mozaffar, M., and Cao, J., 2023, "Efficient GPU-Accelerated Thermomechanical Solver for Residual Stress Prediction in Additive Manufacturing," Comput. Mech., **71**(5), pp. 879–893.

[2] Wang, D., and Chen, X., 2018, "A Multirate Fractional-Order Repetitive Control for Laser-Based Additive Manufacturing," Control Eng. Pract., **77**, pp. 41–51.

[3] Bennett, J., Webster, S., Byers, J., Johnson, O., Wolff, S., Ehmann, K., and Cao, J., 2022, "Powder-Borne Porosity in Directed Energy Deposition," J. Manuf. Process., **80**, pp. 69–74.

[4] Wang, D., and Chen, X., 2021, "Closed-Loop High-Fidelity Simulation Integrating Finite Element Modeling With Feedback Controls in Additive Manufacturing," ASME J. Dyn. Syst. Meas. Contr., **143**(2), p. 021006.

[5] Schwalbach, E. J., Donegan, S. P., Chapman, M. G., Chaput, K. J., and Groeber, M. A., 2019, "A Discrete Source Model of Powder Bed Fusion Additive Manufacturing Thermal History," Addit. Manuf., **25**, pp. 485–498.

[6] Masoomi, M., Thompson, S. M., and Shamsaei, N., 2017, "Laser Powder Bed Fusion of Ti-6Al-4V Parts: Thermal Modeling and Mechanical Implications," Int. J. Mach. Tools Manuf., **118**, pp. 73–90.

[7] Ren, Y., and Wang, Q., 2023, "A Finite Difference Method for Fast Prediction and Control of Part-Scale Temperature Evolution in Laser Powder Bed Fusion," J. Manuf. Process., **93**, pp. 299–314.

[8] Foroozmehr, A., Badrossamay, M., Foroozmehr, E., and Golabi, S., 2016, "Finite Element Simulation of Selective Laser Melting Process Considering Optical Penetration Depth of Laser in Powder Bed," Mater. Des., **89**, pp. 255–263.

[9] Song, L., and Mazumder, J., 2011, "Feedback Control of Melt Pool Temperature During Laser Cladding Process," IEEE Trans. Contr. Syst. Technol., **19**(6), pp. 1349–1356.

[10] Cao, X., and Ayalew, B., 2015, "Control-Oriented MIMO Modeling of Laser-Aided Powder Deposition Processes," American Control Conference (ACC), Chicago, IL, July 1–3, IEEE, pp. 3637–3642.

[11] Fathi, A., Khajepour, A., Durali, M., and Toyserkani, E., 2008, "Geometry Control of the Deposited Layer in a Nonplanar Laser Cladding Process Using a Variable Structure Controller," ASME J. Manuf. Sci. Eng., **130**(3), p. 031003.

[12] Wang, D., Zhao, X., and Chen, X., 2021, "New Hammerstein Modeling and Analysis for Controlling Melt Pool Width in Powder Bed Fusion Additive Manufacturing," ASME Lett. Dyn. Syst. Contr., **1**(3), p. 031012.

[13] Hofman, J., Pathiraj, B., Van Dijk, J., de Lange, D., and Meijer, J., 2012, "A Camera Based Feedback Control Strategy for the Laser Cladding Process," J. Mater. Process. Technol., **212**(11), pp. 2455–2462.

[14] Wang, D., Jiang, T., and Chen, X., 2021, "Control-Oriented Modeling and Repetitive Control in In-Layer and Cross-Layer Thermal Interactions in Selective Laser Sintering," ASME Lett. Dyn. Syst. Contr., **1**(1), p. 011003.

[15] Tang, L., and Landers, R. G., 2011, "Layer-to-Layer Height Control for Laser Metal Deposition Process," ASME J. Manuf. Sci. Eng., **133**(2), p. 021009.

[16] Irwin, J. E., Wang, Q., Michaleris, P. P., Nassar, A. R., Ren, Y., and Stutzman, C. B., 2021, "Iterative Simulation-Based Techniques for Control of Laser Powder Bed Fusion Additive Manufacturing," Addit. Manuf., **46**, p. 102078.

[17] Kannatey-Asibu Jr, E., 2009, *Principles of Laser Materials Processing*, Vol. 4, John Wiley & Sons, Hoboken, NJ.

[18] Tang, M., Pistorius, P. C., and Beuth, J. L., 2017, "Prediction of Lack-of-Fusion Porosity for Powder Bed Fusion," Addit. Manuf., **14**, pp. 39–48.

[19] Chen, X., Jiang, T., Wang, D., and Xiao, H., 2018, "Realtime Control-Oriented Modeling and Disturbance Parameterization for Smart and Reliable Powder Bed Fusion Additive Manufacturing," Annual International Solid Freeform Fabrication Symposium-An Additive Manufacturing Conference, Austin, TX, Aug. 13–15.